Oxidized cellulose nanofibers from sugarcane bagasse obtained by microfluidization: Morphology and rheological behavior

Cibele Carneiro Pessan [a], Juliana Silva Bernardes [b], Sílvia H.P. Bettini [a,c], Edson R. Leite [a,b,d,*]

[a] Federal University of Sao Carlos, Graduate Program in Materials Science and Engineering, Rodovia Washington Luiz, Km 235, 13.565-905 São Carlos, SP, Brazil
[b] Brazilian Nanotechnology National Laboratory (LNNano), Brazilian Center for Research in Energy and Materials (CNPEM), 13083-970 Campinas, SP, Brazil
[c] Federal University of Sao Carlos, Department of Materials Engineering, São Carlos, SP, Brazil
[d] Federal University of Sao Carlos, Department of Chemistry, São Carlos, SP, Brazil

ARTICLE INFO

ABSTRACT

It is advantageous to understand the relationship between cellulose fiber morphology and the rheological behavior of its dispersions so that their application can be optimized. The goal of this study was to produce sugarcane bagasse-sourced cellulose dispersions with different numbers of high-pressure homogenization cycles. Microfluidization produced cellulose nanofibers (between 5 and 80 nm in diameter) with similar surface charge densities and crystallinities (measured on the resulting films). Oscillatory rheology showed that TEMPO-oxidized cellulose dispersions exhibited gel-like behavior. However, not only did the samples with more microfluidization cycles present a lower storage modulus, but the sample with 100 cycles completely lost the gel-like characteristic, presenting a viscous fluid rheological behavior. Thixotropy loop tests revealed the influence of nanofiber length on the dispersion's structure, as evidenced by the decrease in the hysteresis value along with fiber breakage. Therefore, our findings demonstrate that the rheological properties of the dispersion can be tuned according to the length of the nanofibers, allowing for targeted applications.

1. Introduction

Cellulose, the most abundant biopolymer worldwide, can be obtained from bacteria, tunicates, and plant species. Humankind has developed technologies to handle and extract cellulosic materials (CMs) from nature, and their use has continuously evolved and transformed. Today, it includes everything from writing substrate to clothing technology, as well as structural reinforcement components, suspension dispersing and thickening agent, Pickering emulsion, biocompatible material for cell growth, among other functions in the cosmetics, food, medical, transport, gas, and energy industries. Cellulosic materials contribute even more to the industry's needs and interests by addressing sustainability challenges such as sustainable production, as crop byproducts are an important source of CMs (Czaikoski, da Cunha, & Menegalli, 2020).

In addition to sourcing possibilities, the process through which CMs are obtained is of interest. Depending on the intended final application, raw materials can be subjected to a series of chemical or physical processes (or a combination of both), resulting in various CMs. Since its discovery and isolation by Anselme Payen in 1838 (Habibi, Lucia, & Rojas, 2010), many scientists have studied cellulose chemistry and processing methods that allow for the production of tailored CMs. Current production methods can control properties such as purity, hydrophobicity, and particle size, including the production of nanosized cellulose, mostly grouped as nanofibers (CNFs) and nanocrystals (CNCs). While CNCs are obtained through acid hydrolysis, CNFs are mostly obtained via a mechanical route. However, combining chemical and physical processes may facilitate the production of finer materials and may also be necessary to achieve desired properties, such as chemical functionalities (Souza, Mariano, de Farias, & Bernardes, 2019). In line with circular economy concepts, some research groups have focused on delivering high-quality CMs using more sustainable methods, reducing the need for aggressive chemicals, or more energy-efficient methods (Isogai, Saito, & Fukuzumi, 2011; Otoni et al., 2018).

CNFs and CNCs differ from each other regarding their aspect ratio and crystallinity. While acid hydrolysis degrades the amorphous regions, resulting in highly crystalline whisker-like particles (ranging from approximately 5 to 10 nm wide and 50 to 500 nm long), vigorous mechanical disintegration methods can separate smaller bundles of cellulose fibers and expose micro- and nanofibrils, which have both

---

crystalline and amorphous regions along their length (usually 5 to 10 nm wide and several microns long) (Habibi et al., 2010; Moon, Martini, Nairn, Simonsen, & Youngblood, 2010). Mechanical methods include grinding, sonication, high-pressure homogenization, and disintegration via blender or disperser equipment. However, each method applies different degrees of energy to the cellulose, which affects morphology of the fibers (Lavoine, Desloges, Dufresne, & Bras, 2012; Qing et al., 2013). The resulting morphology depends on the combination of pretreatment processes, the subsequent mechanical disintegration techniques used, and the extent of mechanical fibrillation (Li, Wu, Moon, Hubbe, & Bortner, 2021).

For cellulosic nanomaterials (CNMs), the particle's aspect ratio and applied shear rate are critical parameters for the rheological behavior of the resulting dispersions, affecting their performance. The shear-thinning behavior and structural build-up of dispersions after applied stress are of great importance for controlling the fabrication processes of films and filaments, for instance (Wang, Wang, & Xu, 2020).

The microfluidization process used in this work is intended to break the fibrillar structure, exposing cellulose micro- and nanofibrils. It would be expected that with a greater number of cycles, the final width and length of the fibrils would be smaller. However, the aspect ratio of the particles may also be affected, meaning that the process with a greater number of cycles could result in shorter fibrils.

This study investigated how the morphology and the rheological properties of TEMPO-oxidized cellulose dispersions from sugarcane bagasse are affected by the number of cycles of the microfluidization mechanical treatment. Our hypothesis was that there should be an optimal number of cycles of the microfluidization process to which the material can be subjected in order to achieve the width of a single fibril without extensively damaging the fibrils' length. And, because rheological properties are related to the morphology of the fibrils (diameter, length, and aspect ratio), this should reflect on the dispersion's rheological properties. It was also hypothesized that high cycling numbers could reduce the crystallinity of the material. CNFs were characterized by Atomic Force Microscopy (AFM), infrared spectroscopy (FTIR), X-ray Diffraction (XRD), oscillatory rheology, and flow curves.

2. Materials and methods

2.1. Materials

Sugarcane bagasse was supplied by the Brazilian Biorenewables National Laboratory of the Brazilian Centre for Research in Energy and Materials (LNBR – CNPEM, Campinas, SP, Brazil). Chemical materials (TEMPO, NaCl, NaOH, NaBr, HCl, and NaClO) were acquired from Sigma-Aldrich/Merck and Synth. Detailed information on reagent purity and suppliers can be found in Table S1 in the Electronic Supplementary Information (ESI).

2.2. Experimental methods for cellulose extraction and dispersion production

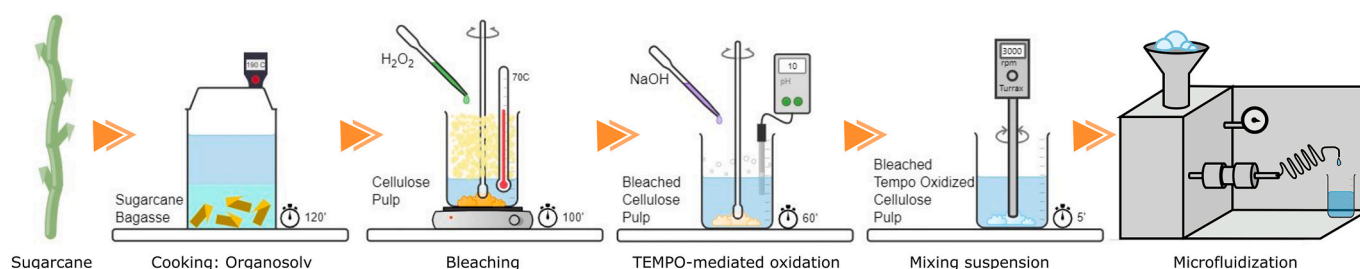Cellulose dispersion production follows a sequence of procedures, briefly illustrated in Fig. 1 (a detailed experimental workflow including all procedures can be found in Fig. S1 in the ESI).

2.2.1. Organosolv pulping reaction

Initially, cellulose from sugarcane bagasse was isolated from biomass using the organosolv pulping method, according to the methodology described in the literature (Oliveira, Bras, Pimenta, Curvelo, & Belgacem, 2016), which extracts soluble organic compounds from the pulp. After washing, sugarcane bagasse (300 g) was placed in a Parr reactor along with an equal-part mixture of ethanol and water (3 L) and cooked at 190 °C and 30 bar for 120 min. After cooling, the pulp was separated from the lignin-rich liquor, blended with NaOH solution (1 % w/w) in a disintegrator, then washed, and sieved until a neutral pH was achieved. Finally, the samples were lightly centrifuged (to remove the excess of water).

2.2.2. Cellulose pulp bleaching

Subsequently, the cellulose pulp was bleached according to the methodology described in the literature (Teixeira et al., 2011), in which H_2O_2 solution (500 mL, 24 % v/v) was slowly and steadily dripped onto a heated (70 °C) mixture of cellulose and NaOH solution (500 mL, 5 % w/v) under continuous mechanical stirring. After cooling, the dispersion was washed and sieved until a neutral pH was achieved.

2.2.3. TEMPO-mediated oxidation of bleached cellulose pulp

The dispersed bleached cellulose underwent TEMPO (0.016 $g/g_{cellulose}$) mediated oxidation, as described in the literature (Saito, Kimura, Nishiyama, & Isogai, 2007)). Cellulose oxidation occurred at pH 10 (controlled by the addition of NaOH solution) in the presence of NaBr (0.1 $g/g_{cellulose}$) and NaClO (5 mmol/$g_{cellulose}$) for 130 min. Afterwards, the pH was neutralized, and the mixture was allowed to rest for 30 min. The dispersion was washed with the aid of centrifugation. The final dispersion presented a 1 wt% solids content.

2.2.4. High pressure homogenization (microfluidization)

Finally, the TEMPO-oxidized cellulose (TOC) and water dispersion were mechanically treated. The equipment used was a MP110 Microfluidizer from Microfluidics, with Z-shaped interaction chambers (H30Z and G10Z, with inner diameters of 200 μm and 87 μm, respectively). The dispersion was cycled through the equipment with one or both chambers assembled at a concentration of 1 wt%, up to 100 times. The denominations of the samples are derived from this process; for example, samples H50 and HG100 are cellulose water dispersions that were cycled through the high-pressure homogenizer 50 times using the H30Z interaction chamber and 100 times using both H30Z and G10Z interaction chambers, assembled sequentially, respectively (all samples' denominations and descriptions are available in Table S2 in ESI).

2.3. Characterization methods

The morphology of the CNMs was characterized using MorFi equipment and AFM. The surface chemical charges of the dispersions were measured using conductometric titration. Structural

Fig. 1. Summarized experimental workflow for cellulose dispersion production.

characteristics of self-standing films were analyzed by XRD and FTIR, and the rheological behavior of the dispersions was studied by oscillatory rheology and thixotropic loop curves.

2.3.1. Chemical and structural characterization

The carboxylate content on the cellulose surface was acquired by conductometric titration of pulp dispersions before and after mechanical treatment, according to an adaptation of the suggested methodologies reported in the literature (Foster et al., 2018; Saito & Isogai, 2004) (measurements were performed in duplicate). The cellulose pulp and CNF dispersion were dispersed in deionized water, and a NaCl solution was added (resulting in a 1 mM NaCl solution). Before titration, the HCl solution was added to the mixture under agitation until the pH value was approximately 3. The dispersion was then titrated with a NaOH solution (0.1 mL steps) under continuous agitation. Temperature and pH values were measured with a pH meter from Hanna Edge and conductivity with a FiveEasy conductivity meter from Mettler Toledo every 10–30 s. Further details on the specifics of the calculation procedure are available in ESI, Fig. S2.

Infrared (FTIR) and X-ray diffraction (XRD) analyses were performed on self-standing cellulose films prepared by casting method. Approximately 6 mL of cellulose dispersion at 1 wt% was spread over a 60 mm diameter Petri dish and vacuum oven dried at 45 °C for at least 8 h, then manually released from the Petri dish. FTIR was performed on a Nicolet 6700 FT-IR spectrometer from Thermo Scientific, from 400 to 4000 cm^{-1} wavelengths, with 64 scans at 2 cm^{-1} resolution, on film transmittance mode. XRD measurements were performed from 5 to 90° (2θ), at a 0.02° step, at a 0.5 s.step^{-1} acquisition rate, in Bragg-Brentano mode, on D8 Advance Eco equipment from Bruker operating at 40 kV and 25 mA, with a Cu Kα radiation of 1.5418 Å.

2.3.2. Rheological characterization

The rheological behavior of the dispersion was characterized using an ARES rheometer from TA Instruments in concentric cylinder geometry (a bob with 31.9 mm and 25 mm length and diameter, respectively, and a cup of 27 mm diameter). An oscillatory strain sweep (from 10^{-1} to 10^1 % strain and 1 rad.s^{-1} frequency) was performed to determine the linear viscoelastic region of the dispersion, and an oscillatory frequency sweep (from 10^{-2} to 10^2 rad.s^{-1} and 1 % strain) was performed to evaluate the dispersion's behavior. A thixotropic loop was performed from 0 to 1000 s^{-1} strain rate, up and downwards. The hysteresis was calculated from the difference between the areas obtained from the integration of the flow curves, ranging from 200 to 1000 s^{-1} (interval chosen to avoid the initial region up to 200 s^{-1}). The hysteresis values are given by Hysteresis [Pa.s^{-1}] = U – D and Hysteresis [%] = 100 % × (U – D) / U, where

$$U = Area_{\int_{200}^{1000}}^{upwards} = \int_{200}^{1000} Shear\ Stress_{upwards} dStrain\ Rate \qquad (1)$$

$$D = Area_{\int_{200}^{1000}}^{downwards} = \int_{200}^{1000} Shear\ Stress_{downwards} dStrain\ Rate \qquad (2)$$

All measurements were performed in triplicate at room temperature (23 °C) with samples that had been resting for at least 8 h, so no manipulation history would have interfered with the measurements.

2.3.3. Morphological characterization

The evolution of the length and diameter of the cellulose fibers after pulping, bleaching, and TEMPO-mediated oxidation processes was measured using a MorFi LB-01 fiber and shive analyzer from Techpap (LGP2). The cellulose pulp was dispersed in water (40 mg in 1 L H$_2$O) and agitated with a T25 ULTRA Turrrax disperser from IKA for 5 min at 3000 rpm. After the microfluidization process, the length and diameter of the cellulose nanofibers were measured using Multimode8 AFM equipment from Bruker in tapping mode. Image analysis was performed using Gwyddion and FIJI softwares.

3. Results and discussion

Sugarcane bagasse was treated for cellulose extraction, bleaching, and oxidation. Fig. 2 shows the appearance of the cellulose pulp after each chemical process. Following this, TOC dispersions were prepared at 1 wt% by microfluidization. A video demonstrating the manipulation of the dispersions is also available in the ESI.

3.1. Chemical and structural characterization

First, conductometric titration was performed on the tempo-oxidized cellulose dispersions before and after high-pressure homogenization. The results reveal that the mechanical treatment did not alter the surface charge density, which remained around 0.9 mmol.g^{-1} of oxidized cellulose before and after the microfluidization process (sample HG25).

The FTIR spectroscopy results of the H50, HG25, HG50, and HG100 film samples are presented in Fig. 3A, in which the absorbance bands of interest are highlighted. The locations of the noteworthy chemical bonds are highlighted in the molecular model of cellulose shown in Fig. 3B, which is further described in Fig. 3C.

Initially, a qualitative analysis of the fingerprint regions of the spectra allowed for the type of cellulose obtained from sugarcane bagasse to be verified as type I (details are available in Fig. S3 in ESI). Quantitative analysis, such as FTIR's Lateral Order Index (LOI – proposed by Hurtubise & Krässig, 1960, also called Crystalline Index by Nelson & O'Connor, 1964a), Total Crystallinity Index (TCI – proposed by Nelson & O'Connor, 1964b), and Hydrogen Bond Intensity (HBI), are useful tools for comparing samples' crystallinity and supramolecular order.

The HBI is related to chain mobility and regularity. It is given by the ratio between the absorbance intensities of the peaks related to νOH stretching vibrations and the in-plane bending vibration of δCH at C6 at 3400–3000 cm^{-1} and 1320–1310 cm^{-1}, respectively. Higher HBI values may indicate a higher water content and/or more packing disorder (Cichosz & Masek, 2020). The LOI (Hurtubise & Krässig, 1960; Nelson & O'Connor, 1964b) was calculated from the ratio between the peaks related to the $\delta_s CH_2$ scissoring motion and νC-O-C stretching vibration, given by A_{1429}/A_{897}. While the A_{1429} band is attributed to more crystalline regions, the A_{897} region is related to the greater mobility of the molecular region, which would indicate lower packing efficiency (Spiridon et al., 2020). The TCI was proposed (Nelson & O'Connor, 1964a) as the ratio of A_{1372}/A_{2900}. The authors related A_{1370} to the δCH bending vibrations of more crystalline regions and A_{2900} to the νCH stretching vibration of less-ordered regions.

Since these FTIR indices can be related to crystallinity values calculated from XRD analysis (Cichosz & Masek, 2020; Czaikoski et al., 2020), the crystallinities of the samples were calculated using Segal's and peak deconvolution methods (Foster et al., 2018; French & Santiago Cintrón, 2013; Nam, French, Condon, & Concha, 2016). Fig. 3D presents FTIR indices (LOI, TCI, and HBI) and XRD Segal's crystallinity values for H50, HG25, HG50, and HG100 film samples (XRD diffractograms are shown in Fig. S3 in ESI).

It has been reported that mechanical treatment can result in lower crystallinity (Liu et al., 2016). However, all samples had similar values for FTIR LOI, TCI, and HBI indices and XRD-calculated crystallinities, indicating that the mechanical treatment, despite being highly aggressive, did not significantly alter the crystallinity proportion and that the breakage most likely occurred on the amorphous region of the fibrils.

3.2. Morphological characterization

The evolution of the particle size distribution during the stages to obtain CNF nanofibers was documented using optical and atomic microscopy techniques.

Fig. 2. Images of cellulose pulp after extraction by organosolv pulping, bleaching, and TEMPO-mediated oxidation (from left to right).

A

$$HBI = \frac{A_{3333}}{A_{1315}}$$

$$TCI = \frac{A_{2894}}{A_{1372}}$$

$$LOI = \frac{A_{1428}}{A_{897}}$$

Legend: ▼ H50, ● HG25, ◆ HG50, ▲ HG100

C Region (cm⁻¹) and Chemical Group

	Region (cm^{-1})	Chemical Group	
i	3350	νO-H	Covalent OH & hydrogen bond
ii	2900	νC-H	
iii	1642		Adsorbed water Hydrogen bonds
iv	1429	δsC-H	at C6 crystalline region
v	1340-1335	δC-O-H	in plane at C2 and C3
vi	1370	δC-H	
vii	1315	δωC-H	at C6
viii	1236	δC-O-H in plane at C6	
ix	1163	νC-O-C B-glycosidic bond	
x	1140	νRing in plane	
xi	1030	νC-O at C6	
xii	897	νC-O-C β-glycosidic bond at amorphous region	
xiii	662	δC-O-H out of plane	

D

	XRD		FTIR		
	Segal's Crystallinity Index	Xc% Peak Area Calculation	LOI	TCI	HBI
H50	66%	84%	1.56	86%	9.61
HG25	70%	85%	1.52	82%	9.98
HG50	71%	85%	1.58	84%	10.77
HG100	72%	85%	1.57	85%	10.70

$X_C(\%) = (A_C / A_T)*100$
$v = Streching\ vibration$
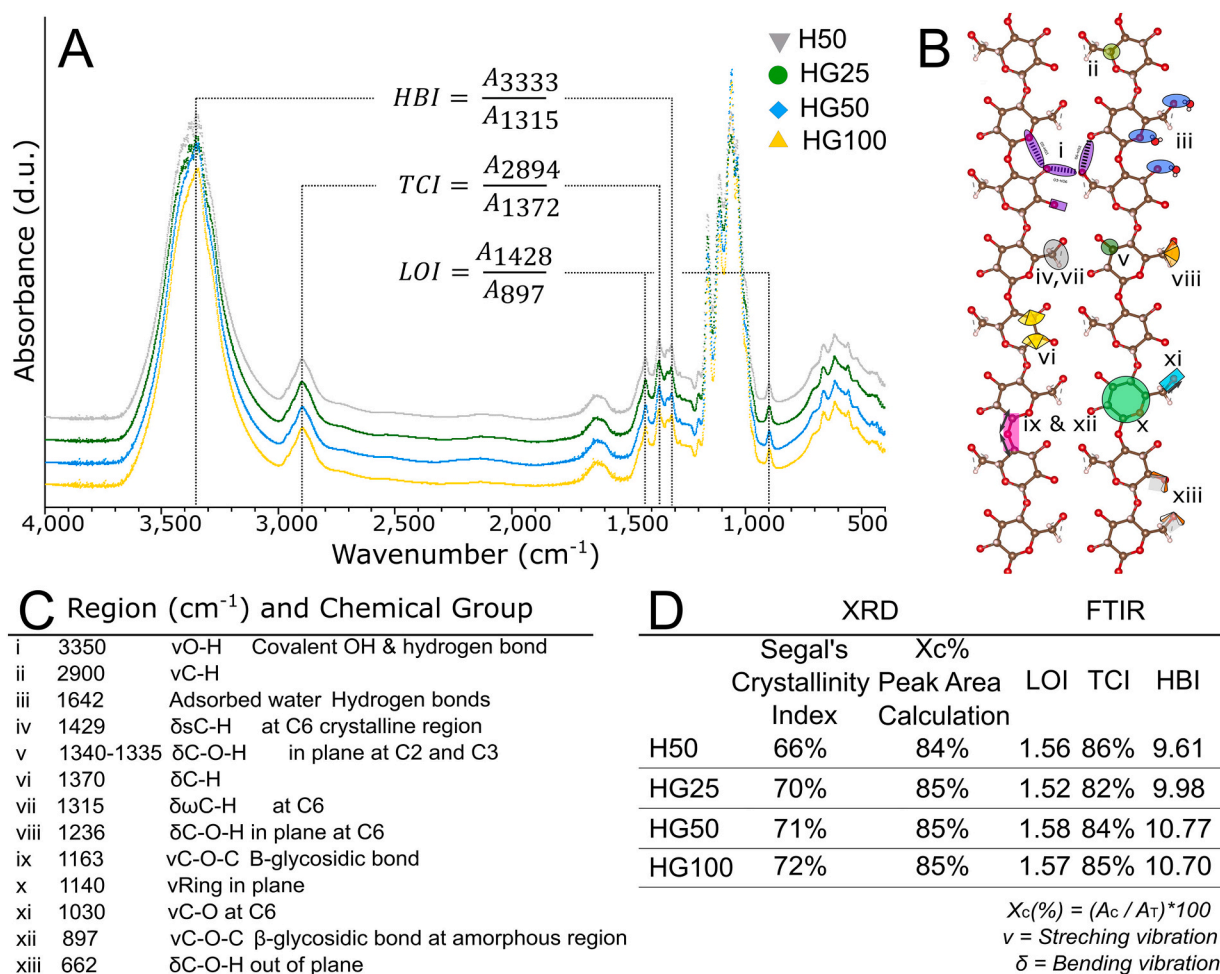$\delta = Bending\ vibration$

Fig. 3. (A) FTIR spectra for TOC films H50, HG25, HG50, and HG100; (B) Illustrative location of chemical bonds of interest responsible for the absorbance bands listed in (C); (D) Results for crystallinity indices calculated from XRD and FTIR measurements.

Cellulose dispersions were analyzed using MorFi and optical microscopy equipment after organosolv pulping, pulp bleaching, TEMPO-mediated oxidation, and microfluidization processes. As shown in Fig. 4, it is possible to follow the evolution of the fibers' size along the experimental sequence. It is noticeable that the chemical processes contributed to the loosening of the fiber bundles, thereby exposing smaller (micro) fibers. However, it was insufficient for obtaining isolated nanofibrils.

The histograms in Fig. 4D show that the length and width distribution profiles remained very similar, with most occurrences at the smallest measurable sizes. This could result from the sensitivity limit of the technique for detecting submicron dispersions. Further details of MorFi's analysis (including dispersion after microfluidization) are described in Figs. S4 and S5 in the ESI.

Continuing to follow the particle size evolution along the next processing stages, AFM was performed on the cellulose dispersions after 2,
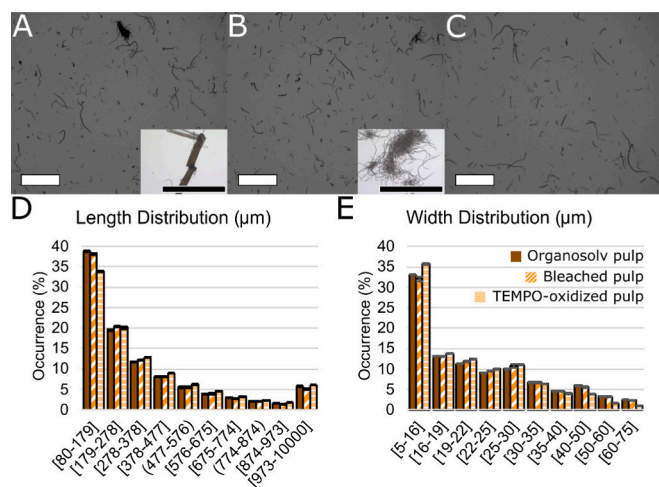
Fig. 4. MorFi images of cellulose dispersion after (A) organosolv pulping, (B) pulp bleaching, and (C) TEMPO-mediated oxidation processes; Optical microscopy inserts in (A) and (B) provide further detail on fiber appearance (all scale bars are 2 mm); Average fiber (D) length and (E) width distribution for each treatment step.

10, 25, 50, and 100 microfluidization cycles. The resulting images, presented in Fig. 5A–D, allowed the measurement of the width and length of the nanofibrils. As shown in Fig. 5F, the diameter distribution became narrower with an increasing number of cycles until the exposure of isolated fibrils at 25 cycles (the average diameter and diameter distribution of samples HG25, HG50, and HG100 were similar). In contrast, the fibril length values (presented in Fig. 5E) continued to decrease, due to longer exposure to high shear stress.

3.3. Rheological characterization

Because CNFs are elongated particles that are abundant in hydrophilic surface groups, their interactions with water are more complex than those of spherical and chemically neutral particles. Considering their use as rheological modifiers in many industries and their potential applications in 3D printing, it is important to study how the processes employed to obtain cellulose dispersions affect their rheological behavior.

Notably, while the rheological behavior of cellulosic dispersions is greatly influenced by the dispersion's concentration and surface functionalization, the chosen geometry for the measurement can also affect the results (Foster et al., 2018). Parallel plates, cone-plane and concentric cylinders geometries are suited to analyze overlapping viscosity ranges, but the results cannot be compared directly, due to geometry-related wall depletion effects (Li et al., 2021). The sample overflowing out of the plate geometry at higher shear rates was the primary reason for choosing concentric cylinders in this study.

Rheological analyses were performed for the H50, HG25, HG50, and HG100 samples. First, an Oscillatory Strain Sweep was performed to define the linear viscoelastic region of the dispersions (Fig. S6 in ESI). The value of 1 % strain was chosen for the oscillatory frequency sweep analysis.

An Oscillatory Frequency Sweep was performed to study the rheological behavior of the dispersions. The shape of the curves and the relationship between the storage modulus (G') and loss modulus (G'') allowed us to identify the nature of the samples (gel, viscoelastic solid, or viscoelastic fluid).

As seen in Fig. 6, most samples exhibit typical gel-like behavior for the oscillatory frequency sweep: i) both the storage (G') and loss (G'') moduli (Figs. 6A and B, respectively) are mostly independent of frequency values; ii) Tan Delta values (Fig. 6C) are always smaller than one. However, the HG100 sample deviates from the gel-like behavior and begins to exhibit viscoelastic liquid-type behavior, where G' and G''
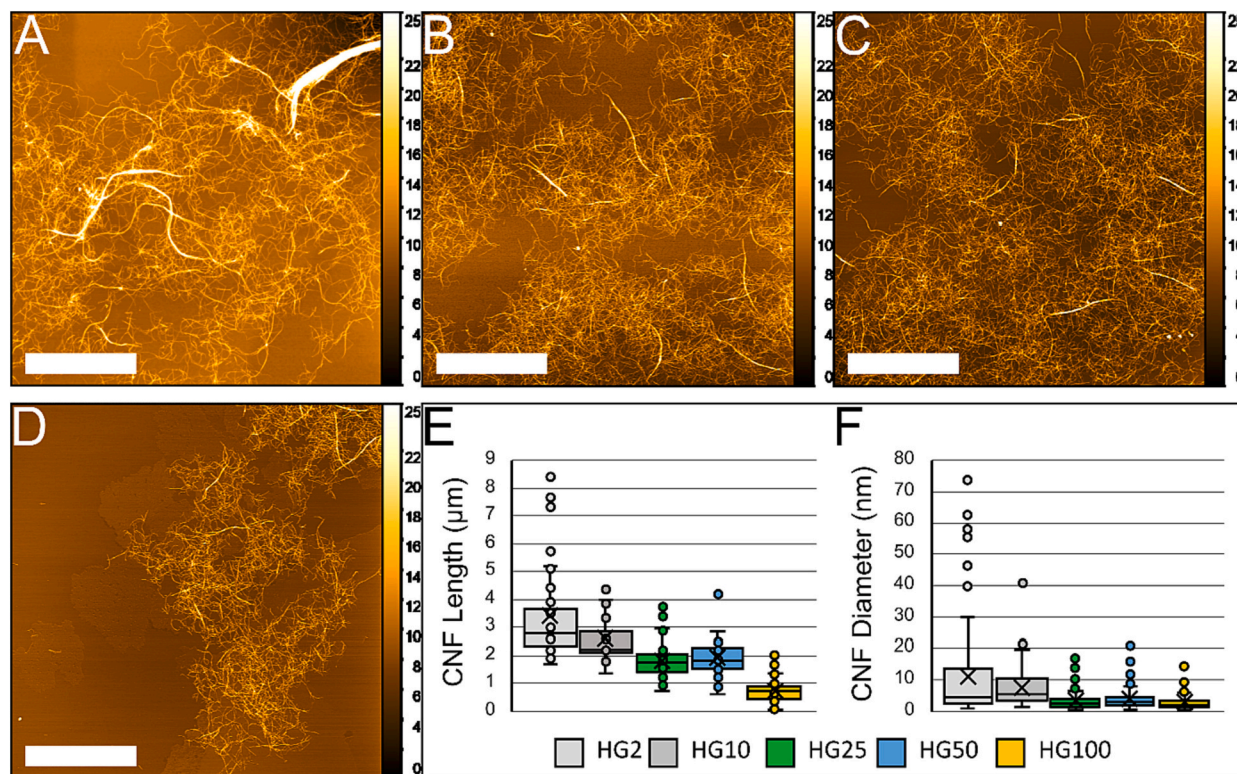
Fig. 5. AFM topographies of cellulose dispersions cycled (A) 2, (B) 25, (C) 50 and (D) 100 times (all scale bars are 3 μm) and boxplot type graphs of measurable (E) length and (F) diameter distributions of dispersions HG2, HG10, HG25, HG50, and HG100.
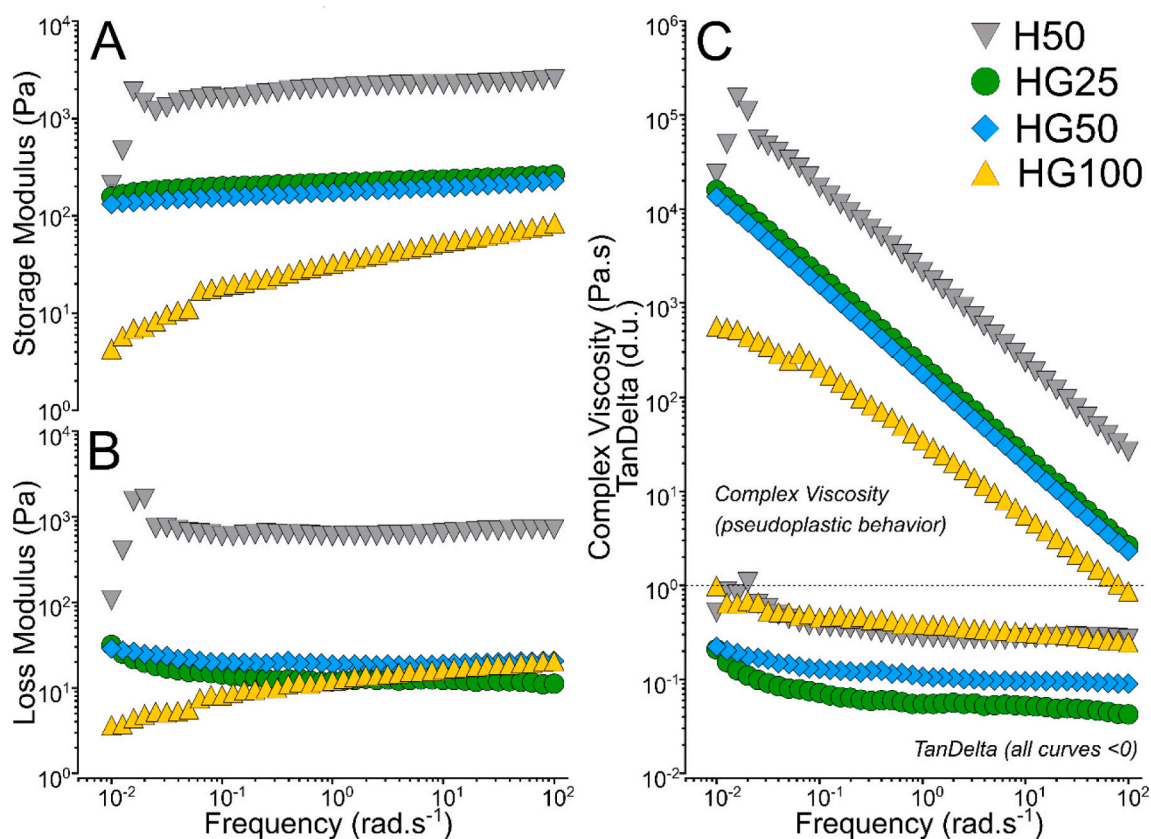
Fig. 6. Oscillatory Frequency Sweep curves: (A) Storage Modulus, (B) Loss Modulus, and (C) Complex Viscosity and Tan Delta versus frequency (performed at 1 % strain).

vary significantly with frequency (Li et al., 2021). As such, we can classify samples H50, HG25, and HG50 as exhibiting gel-like rheological behavior, whereas HG100 approaches the behavior of a viscous fluid. The dependence of the complex viscosity (η^*) on the frequency is also shown in Fig. 6C. According to the Cox-Merz empirical rule, which predicts that complex viscosity and steady shear viscosity are equivalent when the angular frequency and steady shear rate are equal, all

compositions exhibited shear thinning behavior, with decreasing values of viscosity as the number of cycles increased.

Permanent regimen analysis (shear stress response over the applied strain rate) was performed to observe the structural properties of the samples over time. The thixotropic loop test indicates thixotropic behavior rather than measuring the phenomenon itself. This is because the thixotropic loop reveals whether the structural fluid has suffered
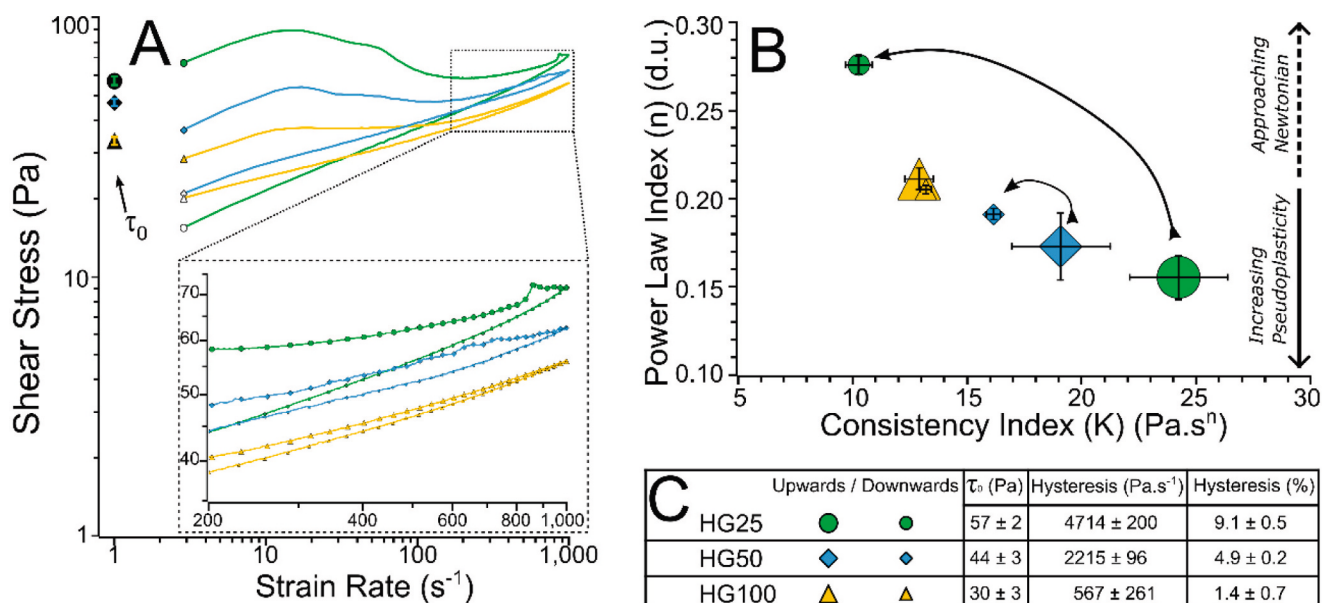

Fig. 7. (A) Thixotropic loop test curves; (B) Power Law index (n) versus consistency (K) from Power Law model fitting of upward and downward flow curves; (C) Calculated values for τ_0 and thixotropic loop hysteresis.

changes in its structure, while the structure's buildup back to its previous form would only appear in a second test after a certain amount of time. As presented in Fig. 7A, the dispersions exhibited thixotropic behavior because the second segment of the thixotropic loop (downward portion) presented lower shear stress values than the first section (upward portion). It can be observed that with the increasing number of microfluidization cycles, the dispersion became less structured, to the point there is no long-range structure left to be disarranged in the case of sample HG100. This is indicated by the decrease of hysteresis area (calculated according to formulas (1) and (2), for the interval from 200 to 1000 s^{-1}) from HG25 to HG50 and finally HG100, where it became difficult to differentiate between the upward and downward curves.

Steady flow curves can be described by mathematical models such as the power law or Herschel-Bulkley method. These are two-parameter shear-rate-dependent stress models that can be used to describe the CNM flow behavior. However, it must be used carefully because it may not accurately predict the effects of the entangled network, which is the case for many CNF dispersions. The Power Law model describes the stress acting over the material (τ) at a level of shear rate (γ) given by $\tau = K \times \gamma^n$, where K is the consistency of the material and n is the power law index. In some cases, the Herschel-Bulkleys model (a combination of the Bingham and power law models), given by $= \tau_0 + K \times \gamma^n$, could be applied, in which case a minimal stress (τ_0) is required to initiate the material's flow. The flow curves were fitted to the power law model, resulting in the indices presented in Fig. 7B. The Herschel Bulkley model was used to calculate the approximate initial resistance to flow of the upward flow curves.

The graph in Fig. 7B presents the consistency and power law index for the upward and downward curves, further illustrating the structural breakdown of the dispersion. The consistency K value relates to the amount of effort necessary to make the material flow, while the n index refers to the pseudoplasticity of the material ($n < 1$), which is how fast the viscosity decreases with an increase in the shear strain rate. Initially, the upward and downward curves were compared. The undisturbed material (upward curve) presents higher consistency and a lower n index, which translates to a more structured and shear-thinning material. The downward curves fitted to lower values of K (less resistant to flow) and a higher n index (heading towards Newtonian purely viscous behavior).

Additionally, when the samples are compared, the difference in consistency (ΔK) and of the n index (Δn) decreases with increasing cycling number until it reaches zero for the HG100 sample. This indicates that HG25 has a more structured dispersion than HG50, whereas HG100 completely loses this property after 100 cycles. Because HG25, HG50, and HG100 have roughly the same fibril diameter, it would be safe to relate the reported rheological behavior to the length of the cellulosic fibrils, rather than their diameter, because the thixotropic behavior in TO-CNFs is attributed to the physical entanglement of fibrils (Czaikoski et al., 2020; Li et al., 2021). Therefore, the lack of structuring and decrease in the degree of thixotropy in sample HG100 are related to its shorter fibril length, which does not allow for a long-range entangled structure.

Interestingly, in sample HG25, the downward flow curve presented a lower K and higher n index than those of sample HG100. This could also be due to longer fibril lengths: once the gel-like structure is broken and the particles are aligned with each other, the dispersion could flow even more smoothly, behaving more like a Newtonian fluid than the HG100 sample.

The results observed should be related to the decrease in nanofibril length, which impacts the long-range mechanical entanglements between nanofibrils, resulting in inferior mechanical properties. Fig. 8 shows a schematic of the entangled CNF network and how it would deform plastically during flow, which does not occur during the oscillatory test because it is performed in the linear viscoelastic region.

After shear is applied, the gel structure deforms and breaks the long-range physical entanglements, resulting in a less viscous dispersion. Subsequently, during a period of rest, the structure builds up again, returning to its entangled state. On the other hand, the short-fiber dispersion did not exhibit gel-like behavior, even when rested. In this case, there is no long-range network to be broken, which explains the coincidental upward and downward flow curves obtained for sample HG100. Another noticeable detail in Fig. 7B is the fact that the downward flow curve for sample HG25 presented a lower consistency (K) than sample HG100 and a higher power law index. In other words, the rheological behavior of sample HG25 is closer to that of water than that of sample HG100. This result could be due to the formation of small short-term fibril aggregates in sample HG100, while sample HG25 aligned more smoothly with flow.

4. General discussion and conclusions

TEMPO-mediated oxidation was performed on cellulose extracted from sugarcane bagasse. Preliminary morphological results showed that the chemical process alone could not produce single fibrils; nanofibers were obtained only after microfluidization cycles.

Titration, FTIR, and XRD analyses did not allow for sample differentiation, supporting the hypothesis that microfluidization acts preferentially over the physical structure of fibrils and is not aggressive enough to impact surface oxidation density. Even though sample HG100 resembled CNC-like particles, the structural results showed that there is no significant difference between the crystallinities of the samples. Microfluidization resulted in nanofibrils of various lengths.
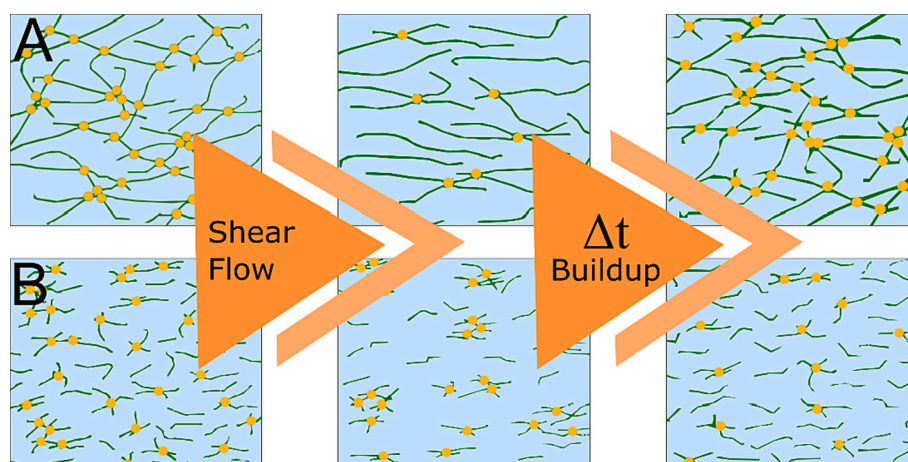

Fig. 8. Schematic figure comparing structural breakup after shear flow and buildup after resting time of (A) long versus (B) short cellulose nanofiber dispersions.

Regarding the nanofibers' morphology, the results showed that the number of cycles affected the aspect ratio of the fibers. Few cycles were able to produce nanofibers; however, with 25 cycles, the elementary single fibril was achieved. With more cycles, shortening of the nanofibrils was observed. The aggressiveness of the microfluidization process allows for the production of CNF but also impacts the fiber's length, which is important for the rheological behavior of the dispersions.

Regarding rheological behavior, it can be seen in Fig. 6 that there is a clear separation between the samples' behaviors. Although samples H50, HG25, and HG50 presented similar results, sample HG100 exhibited inferior moduli and complex viscosity. The results show that 25 and 50 microfluidization cycles with the high shear chamber (HG25 and HG50) produce slightly lower storage modulus dispersion than the 50 microfluidization cycles with the mild interaction chamber (H50). However, the performance is significantly compromised only at 100 cycles, even though elementary nanofibril dimensions and similar diameter distributions have been reached for samples HG25, HG50, and HG100. Similar results are addressed in Fig. 7 with respect to the viscosity of the dispersions. However, the thixotropic loop test provides new information regarding the soundness of the structured liquids. While there is little difference between the HG25 and HG50 samples' oscillatory frequency curves, it becomes visible with the thixotropy loop test, which reveals how differently the dispersions behave during flow. The hysteresis of the flow curves indicates how much more structured sample HG25 is compared to HG100. Along with the initial flow resistance, the upward flow curves exhibited instability at low strain rates, which decreased with increasing cycling number. This phenomenon, known as wall slippage, occurs in fibrous dispersions and is related to the structured network formed by the fibril system (Nechyporchuk, Belgacem, & Pignon, 2014). Consequently, the disappearance of wall slippage in HG100 provides further evidence that HG25 is more structured than HG100.

A better understanding and prediction of the dispersion's behavior during flow is particularly important for processing techniques such as 3D printing. Breaking the dispersion's network allows for easier flow and less plugging, while buildup time is of interest for the mechanical stability and shape integrity of the printed object before drying or chemical setting. The ability to explore this property means tailoring the CNF dispersion's behavior to these types of processing and better adjusting the material's final properties. For this group of samples, we concluded that HG25 would be the best fit for the 3D printing process because it offers the optimum balance between particle alignment during flow and mechanical stability after printing.

Supplementary data to this article can be found online at https://doi.org/10.1016/j.carbpol.2022.120505.

CRediT authorship contribution statement

Cibele Carneiro Pessan: Investigation, Visualization, Writing – original draft. **Juliana Silva Bernardes:** Writing – review & editing, Supervision. **Sílvia H.P. Bettini:** Writing – review & editing, Supervision. **Edson R. Leite:** Writing – review & editing, Supervision.

Declaration of Competing Interest

The authors declare that they have no known competing financial interests or personal relationships that could have appeared to influence the work reported in this paper.

Data availability

Data will be made available on request.

Acknowledgements

References

Cichosz, S., & Masek, A. (2020). IR study on cellulose with the varied moisture contents: Insight into the supramolecular structure. *Materials, 13*(20), 1–22. https://doi.org/10.3390/ma13204573

Czaikoski, A., da Cunha, R. L., & Menegalli, F. C. (2020). Rheological behavior of cellulose nanofibers from cassava peel obtained by combination of chemical and physical processes. *Carbohydr. Polym., 248*(July), Article 116744. https://doi.org/10.1016/j.carbpol.2020.116744

Foster, E. J., Moon, R. J., Agarwal, U. P., Bortner, M. J., Bras, J., Camarero-Espinosa, S., Chan, K. J., Clift, M. J. D., Cranston, E. D., Eichhorn, S. J., Fox, D. M., Hamad, W. Y., Heux, L., Jean, B., Korey, M., Nieh, W., Ong, K. J., Reid, M. S., Renneckar, S. Youngblood, J., … (2018). Current characterization methods for cellulose nanomaterials. *Chemical Society Reviews, 47*(8), 2609–2679. https://doi.org/10.1039/c6cs00895j

French, A. D., & Santiago Cintrón, M. (2013). Cellulose polymorphy, crystallite size, and the segal crystallinity index. *Cellulose, 20*(1), 583–588. https://doi.org/10.1007/s10570-012-9833-y

Habibi, Y., Lucia, L. A., & Rojas, O. J. (2010). Cellulose nanocrystals: Chemistry, self-assembly, and applications. *Chemical Reviews, d*(6), 3479–3500. https://doi.org/10.1021/cr900339w

Hurtubise, F. G., & Krässig, H. (1960). Classification of fine structural characteristics in cellulose by infared spectroscopy. Use of potassium bromide pellet technique. *Analytical Chemistry, 32*(2), 177–181. https://doi.org/10.1021/ac60158a010

Isogai, A., Saito, T., & Fukuzumi, H. (2011). TEMPO-oxidized cellulose nanofibers. *Nanoscale, 3*(1), 71–85. https://doi.org/10.1039/C0NR00583E

Lavoine, N., Desloges, I., Dufresne, A., & Bras, J. (2012). Microfibrillated cellulose - its barrier properties and applications in cellulosic materials: A review. *Carbohydrate Polymers, 90*(2), 735–764. https://doi.org/10.1016/j.carbpol.2012.05.026

Li, M. C., Wu, Q., Moon, R. J., Hubbe, M. A., & Bortner, M. J. (2021). Rheological aspects of cellulose nanomaterials: Governing factors and emerging applications. *Advanced Materials, 33*(21), 1–38. https://doi.org/10.1002/adma.202006052

Liu, C., Li, B., Du, H., Lv, D., Zhang, Y., Yu, G., Mu, X., & Peng, H. (2016). Properties of nanocellulose isolated from corncob residue using sulfuric acid, formic acid, oxidative and mechanical methods. *Carbohydrate Polymers, 151*, 716–724. https://doi.org/10.1016/j.carbpol.2016.06.025

Moon, R. J., Martini, A., Nairn, J., Simonsen, J., & Youngblood, J. (2010). Cellulose nanomaterials review: Structure, properties and nanocomposites. *Chemical Society Reviews, 40*(7), 3941–3994. https://doi.org/10.1039/c0cs00108b

Nam, S., French, A. D., Condon, B. D., & Concha, M. (2016). Segal crystallinity index revisited by the simulation of X-ray diffraction patterns of cotton cellulose Iβ and cellulose II. *Carbohydrate Polymers, 135*, 1–9. https://doi.org/10.1016/j.carbpol.2015.08.035

Nechyporchuk, O., Belgacem, M. N., & Pignon, F. (2014). Rheological properties of micro-/nanofibrillated cellulose suspensions: Wall-slip and shear banding phenomena. *Carbohydrate Polymers, 112*, 432–439. https://doi.org/10.1016/j.carbpol.2014.05.092

Nelson, M. L., & O'Connor, R. T. (1964a). Relation of certain infrared bands to cellulose crystallinity and crystal lattice type. Part II. A new infrared ratio for estimation of crystallinity in celluloses I and II. *Journal of Applied Polymer Science, 8*(3), 1325–1341. https://doi.org/10.1002/app.1964.070080323

Nelson, M. L., & O'Connor, R. T. (1964b). Relation of certain infrared bands to cellulose crystallinity and crystal latticed type. Part I. Spectra of lattice types I, II, III and of amorphous cellulose. *Journal of Applied Polymer Science, 8*(3), 1311–1324. https://doi.org/10.1002/app.1964.070080322

Oliveira, F. B.d., Bras, J., Pimenta, M. T. B., Curvelo, A. A.d. S., & Belgacem, M. N. (2016). Production of cellulose nanocrystals from sugarcane bagasse fibers and pith. *Industrial Crops and Products, 93*, 48–57. https://doi.org/10.1016/j.indcrop.2016.04.064

Otoni, C. G., Carvalho, A. S., Cardoso, M. V. C., Bernardinelli, O. D., Lorevice, M. V., Colnago, L. A., Loh, W., & Mattoso, L. H. C. (2018). High-pressure microfluidization as a green tool for optimizing the mechanical performance of all-cellulose composites. *ACS Sustainable Chemistry and Engineering, 6*(10), 12727–12735. https://doi.org/10.1021/acssuschemeng.8b01855

Qing, Y., Sabo, R., Zhu, J. Y., Agarwal, U., Cai, Z., & Wu, Y. (2013). A comparative study of cellulose nanofibrils disintegrated via multiple processing approaches. *Carbohydrate Polymers, 97*(1), 226–234. https://doi.org/10.1016/j.carbpol.2013.04.086

Saito, T., & Isogai, A. (2004). TEMPO-mediated oxidation of native cellulose. The effect of oxidation conditions on chemical and crystal structures of the water-insoluble fractions. *Biomacromolecules, 5*(5), 1983–1989. https://doi.org/10.1021/bm0497769

Saito, T., Kimura, S., Nishiyama, Y., & Isogai, A. (2007). Cellulose nanofibers prepared by TEMPO-mediated oxidation of native cellulose. *Biomacromolecules, 8*(8), 2485–2491. https://doi.org/10.1021/bm0703970

Souza, S. F., Mariano, M., de Farias, M. A., & Bernardes, J. S. (2019). Effect of depletion forces on the morphological structure of carboxymethyl cellulose and micro/nano cellulose fiber suspensions. *Journal of Colloid and Interface Science, 538*, 228–236. https://doi.org/10.1016/j.jcis.2018.11.096

Spiridon, I., Anghel, N., Dinu, M. V., Vlad, S., Bele, A., Ciubotaru, B. I., Verestiuc, L., & Pamfil, D. (2020). Development and performance of bioactive compounds-loaded cellulose/collagen/ polyurethane materials. *Polymers, 12*(5). https://doi.org/10.3390/POLYM12051191

Teixeira, E.d. M., Bondancia, T. J., Teodoro, K. B. R., Corrêa, A. C., Marconcini, J. M., & Mattoso, L. H. C. (2011). Sugarcane bagasse whiskers: Extraction and characterizations. *Industrial Crops and Products, 33*(1), 63–66. https://doi.org/10.1016/j.indcrop.2010.08.009

Wang, X., Wang, Q., & Xu, C. (2020). Nanocellulose-based inks for 3d bioprinting: Key aspects in research development and challenging perspectives in applications—a mini review. *Bioengineering, 7*(2). https://doi.org/10.3390/bioengineering7020040